

JGR Atmospheres

RESEARCH ARTICLE

10.1029/2020JD033735

Special Section:

A New Era of Lightning
Observations From Space

Key Points:

- Features of luminosity from a lightning flash detected by Atmosphere-Space Interactions Monitor, Geostationary Lightning Mapper, and Lightning Imaging Sensor are related with leader development and cloud properties
- Surges in 777.4 nm luminosity are associated with return stroke currents, continuing currents, recoil leaders, and leader branching
- Altitude of lightning leaders, cloud particles above lightning channels as well as channel luminosity influence the detection of light

Correspondence to:

J. Montanyà,
montanya@ee.upc.edu

Citation:

Montanyà, J., López, J. A., Morales Rodríguez, C. A., van der Velde, O. A., Fabró, F., Pineda, N., et al. (2021). A simultaneous observation of lightning by ASIM, Colombia-Lightning Mapping Array, GLM, and ISS-LIS. *Journal of Geophysical Research: Atmospheres*, 126, e2020JD033735. <https://doi.org/10.1029/2020JD033735>

Received 20 AUG 2020
Accepted 22 JAN 2021

Author Contributions:














Formal analysis: Joan Montanyà, Jesús A. López, Carlos A. Morales Rodríguez

Investigation: Joan Montanyà, Oscar A. van der Velde

Methodology: Joan Montanyà, Carlos A. Morales Rodríguez

Resources: Ferran Fabró, Nicolau Pineda, Javier Navarro-González, Víctor Reglero, Torsten Neubert, Olivier Chanrion, Nikolai Østgaard, Alfonso Ladino-Rincon, David Romero, Glòria Solà, Ricard Horta, Modesto Freijó

A Simultaneous Observation of Lightning by ASIM, Colombia-Lightning Mapping Array, GLM, and ISS-LIS

Joan Montanyà¹ , Jesús A. López¹ , Carlos A. Morales Rodríguez² , Oscar A. van der Velde¹ , Ferran Fabró^{1,3} , Nicolau Pineda^{1,3} , Javier Navarro-González⁴ , Víctor Reglero⁴ , Torsten Neubert⁵ , Olivier Chanrion⁵ , Steven J. Goodman⁶ , Nikolai Østgaard⁷ , Alfonso Ladino-Rincon⁸, David Romero¹, Glòria Solà¹, Ricard Horta¹ , and Modesto Freijó¹

¹Department of Electrical Engineering, Lightning Research Group, Polytechnic University of Catalonia (UPC), Terrassa, Spain, ²Departamento de Ciências Atmosféricas, Instituto de Astronomia, Geofísica e Ciências Atmosféricas, Universidade de São Paulo, São Paulo, Brazil, ³Meteorological Service of Catalonia, Barcelona, Spain, ⁴Image Processing Laboratory, University of Valencia, Valencia, Spain, ⁵National Space Institute, Technical University of Denmark, (DTU-Space), Kgs. Lyngby, Denmark, ⁶Thunderbolt Global Analytics, Owens Cross Roads, AL, USA, ⁷Department of Physics and Technology, Birkeland Centre for Space Science, University of Bergen, Bergen, Norway, ⁸Department of Atmospheric Sciences, University of Illinois, Urbana, IL, USA

Abstract The Atmosphere-Space Interactions Monitor (ASIM) on the International Space Station (ISS) provides optical radiances and images of lightning flashes in several spectral bands. This work presents a lightning flash simultaneously observed from space by ASIM, the Geostationary Lightning Mapper (GLM) and the Lightning Imaging Sensor on the International Space Station (ISS-LIS); and from ground by the Colombia-Lightning Mapping Array (Colombia-LMA). Volumetric weather radar provides reflectivity data to help to interpret the effects of the cloud particles on the observed optical features. We found that surges in radiance in the band at 777.4 nm appear to be related mostly with lightning processes involving currents as well with branching of lightning leaders with new leader development. In cloud areas with reflectivity <18 dBZ above the lightning leader channels at altitudes >7 km, these have been imaged by ASIM and GLM. But in the region with reflectivity <23 dBZ above the lightning leader channels, despite its lower cloud tops and similar altitudes of lightning channels, these have been almost undetectable. The calculated relative optical depths are consistent with the observed optical intensity at the cloud top. Despite the effects of the cloud particles and the altitude of the lightning channels on the attenuation of the luminosity, the luminosity of the lightning channels due to different processes is fundamental for the imaging of lightning from space.

1. Introduction

In the near future, much of the Earth's lightning activity will be continuously monitored from space by lightning imagers placed in geostationary orbit. These new satellite-based instruments open a new era of weather monitoring and research into the role of thunderstorm processes in the dynamics of the atmosphere and in climate change. The Geostationary Lightning Mapper (GLM) on the first of the Geostationary Operational Environmental Satellite GOES-R Series (GOES-16 at 75.2 W) is the first lightning detector in geostationary orbit (Goodman et al., 2013; Rudlosky et al., 2019a, 2019b). GLM is based on its predecessors, the Optical Transient Detector (OTD) and Lightning Imaging Sensor (LIS) Boccippio et al., 2002, Christian et al., 1989). In China, the Lightning Mapping Imager (LMI) on the Feng-Yun4 is detecting lightning in Asia (Yang et al., 2017) and in the near future, Europe and Africa will be continuously monitored by the Lightning Imager (LI) on the Meteosat Third Generation satellites (MTG) (Stuhlmann et al., 2005). All of these systems, new to the geostationary orbit, use optical imagers at the narrow spectral line at the 777.4 nm infrared emission of atomic oxygen that is associated with hot lightning channels (e.g., Soler et al., 2020).

The Atmosphere-Space Interactions Monitor (ASIM) on the International Space Station (ISS) consists of a suite of optical instruments and X-ray and gamma-ray detectors for investigating lightning, Transient Luminous Events (TLEs) and Terrestrial Gamma-ray Flashes (TGFs) (e.g., Chanrion et al., 2019; Neubert et al., 2019). ASIM is equipped with three photometers at 180–230 nm, 337.0 and 777.4 nm spectral bands plus two one-megapixel cameras at 337.0 and 777.4 nm. The objective of the 337.0 nm (blue) and 777.4 nm

Software: Joan Montanyà, Jesús A. López, Ferran Fabró, Javier Navarro-González

Writing – original draft: Joan Montanyà, Steven J. Goodman, Nikolai Østgaard

Writing – review & editing: Oscar A. van der Velde, Nicolau Pineda, Torsten Neubert

(red) instruments is to quantify optical energy leaving from the top of the clouds and to provide images of lightning events. The selected red (777.4 nm) band monitors the emission from neutral atomic oxygen caused by lightning processes like the return stroke and recoil leader events (e.g., Thomas et al., 2000) whereas the blue (337.0 nm) emissions are characteristic of the N₂ second positive system (SPS) which are common in electrical discharges but have been little investigated in lightning. Recently, Soler et al. (2020) have shown blue optical emissions with absence of red to be related with narrow-bipolar events. In these cases, the blue emission is considered to be produced by cold electrical discharges like streamers. In addition to the red and blue channels, the selected far UV (180–230 nm) channel allows the discrimination of TLEs in the higher atmosphere since the optical emissions in this band coming from the troposphere (e.g., from lightning) would be highly attenuated. Because ASIM instruments provide high temporal and spatial resolution of optical activity in the clouds with additional spectral bands. ASIM offers an opportunity to explore in more detail the performance of the lightning imagers in geostationary orbit (e.g., van der Velde et al., 2020). The comparison of data from ASIM in the low-Earth-orbit of the ISS (~400 km, 51.6° inclination) to the geostationary instruments is facilitated by a LIS instrument, also on the ISS (Blakeslee et al., 2020).

The optical emission from lightning that escapes from a cloud is highly affected by scattering and absorption of photons by cloud particles which reduce the signal intensity, and broadens emissions in space and time (e.g., Brunner & Bitzer, 2020; Koshak et al., 1994; Light et al., 2001; Luque et al., 2020; Peterson, 2014; 2019; Thomason & Krider, 1982). This effect has been the subject of several studies that compare detection from space with data from lightning detection systems at ground. In particular, the measurements of Lightning Mapping Array (LMA) networks (Rison et al., 1999) have been useful because they provide 3D reconstructions of lightning leader development inside the clouds. The early comparisons between LIS and LMA (Thomas et al., 2000) showed that most of the detected optical events were associated with lightning channels at the upper part of the storms. Cloud-to-ground (CG) flashes confined to mid and lower altitudes were less detected. In addition, the strongest light emissions were identified to be related with impulsive high current events from recoil leader activity. Most of the works comparing space-based optical detections and LMA flash data focused on the evaluation of the detection efficiency (e.g., Erdmann et al., 2020; Montanyà et al., 2019; Zhang & Cummins, 2020). In these works, only lightning is considered but not the microphysical characteristics of the clouds in which lightning flashes are immersed and their effect on to the propagation of light. Recently, Rutledge et al. (2020) has incorporated radar, GOES ABI and LMA data to evaluate GLM. In this study, it has been identified that GLM detection efficiency depends on the lightning flash geometric size, in agreement with Zhang and Cummins (2020), and the cloud water path. The size of the flash was found to be correlated with the optical brightness whereas the cloud water path was related to the optical extinction. The cloud water path, in turn, depends on the height of the flash that was derived from LMA clustered data and the cloud water content. Using radar, the mean precipitation-sized hydrometeor ice water paths were determined but, with S-band radars, cloud particles cannot be detected. The authors pointed out that despite the small surface areas of cloud particles compared to precipitation-sized ones, their greater concentrations can provide more attenuation of optical energy. In the present work we complement the previously introduced works by relating lightning processes and cloud properties in a LMA flash case observed with the high resolution ASIM photometers and cameras.

This study presents the first report of a lightning flash occurring in a location with simultaneous coverage by the optical photometers and cameras of ASIM, the Colombia-LMA, the GOES-16 Advanced Baseline Imager (ABI), weather radar data, the GLM, and the ISS-LIS. The flash occurred on November 22, 2018 at 08:57:21.4413 UT. We analyze the measurements of the ASIM, GLM, and ISS-LIS instruments relative to the lightning propagation detected by the LMA and the influence of cloud properties estimated from weather radar data. The object of the analysis is to identify the relation of the red and blue optical emissions with different lightning processes and the effects of the cloud properties on the measured luminosity.

2. Data

As ground support for the ASIM mission, the group at the Polytechnic University of Catalonia (UPC) installed one LMA in the Ebro river delta in North-Eastern Spain and another in Colombia (López et al., 2019; van der Velde & Montanyà, 2013). At the time of the event, the Colombia-LMA was composed of six stations

close to the city of Barrancabermeja ($\sim 7^{\circ}\text{N}$, 73.85°W) in Colombia. The LMA system detects sources of radio emissions in the very high frequency range (VHF, 30–300 MHz) that originate from the breakdown processes related to the propagation of lightning leaders. The sources are located in three dimensions using the time-of-arrival technique. Detailed information about the LMA can be found in Rison et al. (1999) and Thomas et al. (2004).

The Modular Multispectral Imaging Array (MMIA) optical sensors of ASIM are three photometers at 180–230 nm (UV), 337.0 nm (4 nm bandwidth) (hereafter the blue signal), and 777.4 nm (5 nm bandwidth) (hereafter the red signal) at $10\ \mu\text{s}$ resolution, and two cameras with $1,000 \times 1,000$ pixels and 12 frames per second at 337.0 nm (5 nm bandwidth) and 777.4 nm (3 nm bandwidth). The angle of view of the blue and red photometers is 80° with a square sensor. The UV photometer has a circular sensor with an angle of view of 80° . The spatial resolution of the cameras is ~ 400 m per pixel toward nadir. A more detailed description of the instruments is found in Chanrion et al. (2019) and in van der Velde et al. (2020).

The Geostationary Lightning Mapper (GLM) and the Lightning Imaging Sensor (ISS-LIS) provide locations of the sources (events) of luminosity for the investigated lightning flash with 2 ms resolution (GOES-R Algorithm Working Group and GOES-R Series Program, 2018). The minimum pixel footprints of GLM and ISS-LIS imagers are 8 and 4 km, respectively. Radiance at the measured 777.4 nm narrow band for each event is provided.

Cloud-to-ground (CG) lightning locations and peak currents are provided by the Keraunos SAS LINET type lightning network in Colombia (Aranguren et al., 2017; Betz et al., 2009) and by the World-Wide Lightning Location Network (WLLN, e.g., Rodger et al., 2006). Additionally, extremely low frequency (ELF) magnetic fields (< 0.01 –300 Hz) measured by the UPC Schumann resonance station in Cape Verde (16.73°N , 22.93°W) are used to identify the presence of continuing currents for those transient events superimposed over the continuous Schumann resonance background (e.g., Boccippio et al., 1995; Burke & Jones, 1996; Huang et al., 1999).

Finally, radar reflectivity (Z) products are provided by the dual polarization C-band Doppler weather radar located in Barrancabermeja of the Colombian Instituto de Hidrología, Meteorología y Estudios Ambientales (IDEAM). It makes volumetric measurements every 8 min with six elevations and a gate resolution of 100 m Cáceres-Leon (2017). Although the radar scan strategy was configured to sample the precipitation, the highest two elevations were able to measure heights from 8 to 17 km for distances from 30 to 67 km where the investigated flash occurred. The derived products used in this study are the maximum Z (Z_{max}), which corresponds to the maximum Z observed in the column at the gate position, and the contoured-frequency-altitude diagram (CFAD) of Z along the corresponding locations of lightning leaders during ASIM video frames. The CFAD (Yuter & Houze, 1995) is a two-dimensional histogram of radar reflectivity with height. The CFADs provide information on changes in the vertical distribution of radar reflectivity that help to identify the cloud depth and hydrometeors types above the altitude of the lightning leaders. For instance, narrow distributions with height imply homogenous precipitating sized particles, while bimodal or broad distributions mean different types or size of hydrometeors.

3. Results

On November 22, 2018, a lightning flash occurred at 08:57:21.4413 UT near Barrancabermeja (Colombia) at $\sim 7.4^{\circ}$ latitude and -73.85° longitude (Figure 1). The flash was in a cell of a large nighttime thunderstorm system within the coverage of the Colombia-LMA in Barrancabermeja and ranging from 36 to 67 km from the radar. The initial part of the flash was outside the field of view of the MMIA sensors (white markers in the south-east view in Figures 1a and 1b) in a region with cloud top temperatures between -73 and -75°C , corresponding to heights of ~ 14.5 km according to ERA-INTERIM reanalysis (Dee et al., 2011). The part of the flash observed by ASIM (Figure 1c and black filled markers in Figures 1a and 1b) mostly developed in a less deep region with warmer cloud top temperatures of -66 to -68°C (~ 13.5 km). For later analysis, the five regions (boxes) depicted in Figures 1b and 1c will be used to relate features of optical observations with lightning processes and cloud properties.

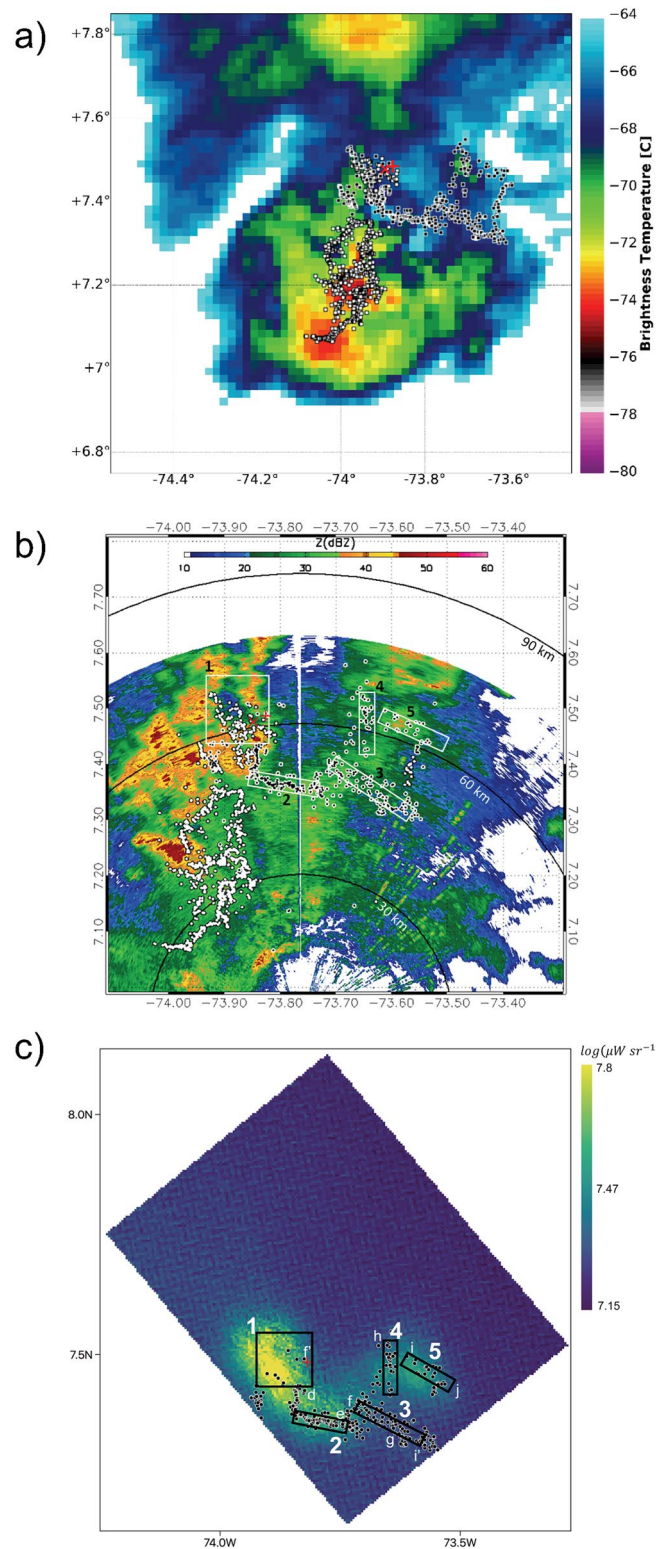


Figure 1. (a) GOES-16 infrared satellite image overlaid with LMA sources. (b) Maximum reflectivity Z_{max} and LMA sources. White filled circles correspond to LMA sources before ASIM video frame 1 and after frame 4. Black filled squares are LMA sources in the field of view of MMIA. The white squares and the numbers indicate the five analyzed areas of interest (boxes). (c) Composition of 777.4 nm (red) MMIA camera stacked frames with the indication of the five considered areas, LMA sources d and the markers (letters) are used to identify the leaders during the period of the video frames. LINET Cloud-to-ground strokes: negative (x), positive (+). GEOS, Geostationary Operational Environmental Satellite; LMA, Lightning Mapping Array; ASIM, The Atmosphere-Space Interactions Monitor; MMIA, The Modular Multispectral Imaging Array.

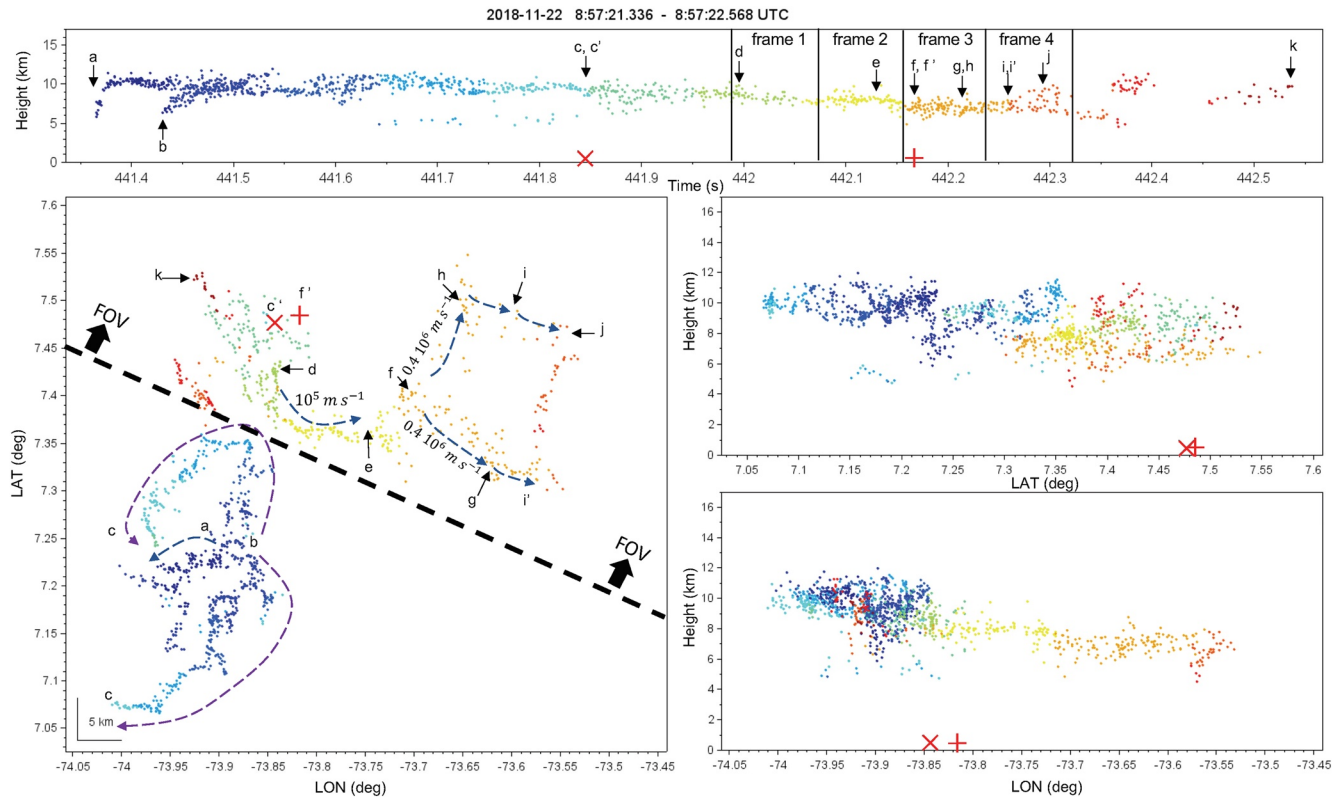


Figure 2. LMA data of the flash on November 22, 2018 at 08:57:21.4413 UT. The top panel is altitude of LMA sources versus time (seconds); the left panel is a plan view map; the panels at the right show altitude (km) by latitude and longitude. LMA sources are colored by time. Markers *a* to *k* are used as reference in the text. LINET cloud-to-ground strokes (red symbols: \times negative, $+$ positive). The exposure times of the four MMIA video frames are indicated as well the part of the field of view (FOV) of MMIA. LMA, Lightning Mapping Array; MMIA, The Modular Multispectral Imaging Array.

3.1. The Lightning Flash

The flash originated at $7.223^{\circ}/-73.91^{\circ}$ in the coldest cloud top (marker *a* in Figure 2). LMA sources in Figure 2 show that the flash initiation was at a height of 5 km with a negative leader propagating upwards at $\sim 10^5 \text{ m s}^{-1}$ up to 11 km. After $\sim 50 \text{ ms}$ (*b*), new negative leaders appeared at the same location as the previous one and expanded simultaneously to southward and northward directions for 450 ms (*b*–*c*). During this period, sources associated with positive leader breakdown were identified at a lower level, $\sim 5 \text{ km}$ altitude. The negative and positive leaders during the first 500 ms period of the flash (*a*–*c*) revealed the existence of positive polarity electric charge between 6 and 11 km altitude and negative electric charge below 5 km.

At 441.85 s new IC breakdown occurred at the north-end of the flash (*c'*) at the time when a negative CG ($-$ CG) stroke of -24 kA was detected by LINET and WLLN. From the location of the $-$ CG stroke, slow negative leaders ($< 10^5 \text{ m s}^{-1}$) expanded radially 5 km for 150 ms (*c'*–*d* and LMA sources in Box 1, Figure 1). After this time (*d*), a fast negative leader ($\sim 10^5 \text{ m s}^{-1}$) was initiated from this area and propagated toward the east into a stratiform region for about 175 ms (*d*–*f*) and progressively descending from 9 to 7 km altitude branching 40 ms (*e*) before ending (sources in Box 2, Figure 1). After the end of this leader (*f*), a positive $+$ CG stroke with 11 kA occurred close to the location (*f'*) of the earlier $-$ CG stroke. As can be deduced from the presence and characteristics of the ELF transient waveform, the initiation of fast intracloud negative leaders (van der Velde et al., 2014; van der Velde & Montanyà, 2013) and using a similar optical discrimination criterion as Bitzer (2017), we assume that this $+$ CG produced continuing current. During this continuing current phase, a fast horizontal negative leader ($0.4 \cdot 10^6 \text{ m s}^{-1}$) at $< 7 \text{ km}$ extended the propagation of the flash further east (*g*–*h*). This leader presented two branches extending simultaneously toward the south-east (*f*–*g* and Box 3, Figure 1) and to the north (*f*–*h* and Box 4, Figure 1). From the leader at the north, a branch propagated at $0.5 \times 10^6 \text{ m s}^{-1}$ toward the north-east (*h*–*j* and Box 5, Figure 1). The flash

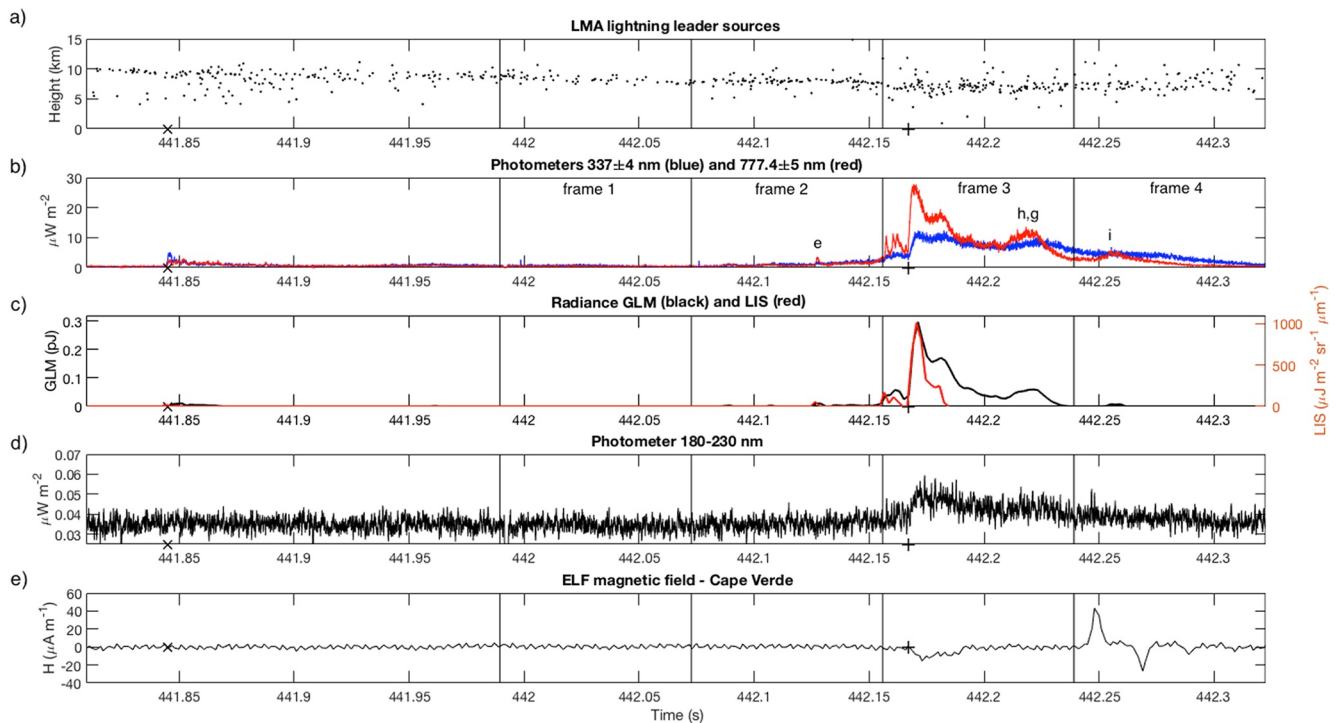


Figure 3. (a) LMA; (b) ASIM 337/4 nm (blue) and 777.3/5 nm (red) including the reference markers (letters); (c) 2 ms-integrated radiances of GLM (black) and ISS-LIS (red); (d) MMIA 180–230 nm (UV) photometer; (e) Magnetic field measured at the UPC's Cape Verde ELF station. Vertical lines indicate the times of the MMIA video frames 1–4. LMA, Lightning Mapping Array; ASIM, The Atmosphere-Space Interactions Monitor; GLM, Geostationary Lightning Mapper; MMIA, The Modular Multispectral Imaging Array; UV, University of Valencia; UPC, Polytechnic University of Catalonia; ELF, extremely low frequency.

ended with the end of this leader propagation followed by a short-isolated breakdown (k) at the north-east of the two CG locations.

In summary, this two-stroke bipolar CG flash started in a convective core of the storm with leaders propagating for 500 ms. A –CG stroke occurred at the north-end of the previous leader activity followed by negative leader propagation into the stratiform region of the cloud for 300 ms. A +CG stroke followed at the location of the previous –CG stroke. This +CG stroke produced continuing current likely supplied by the propagation of a fast negative leader.

3.2. MMIA Photometer, GLM, and ISS-LIS Radiances

Altitudes of the located LMA sources versus time during MMIA detections are plotted in Figure 3a. Radiances measured by MMIA in the three spectral bands (337.0, 777.4, and 180–230 nm) are depicted in Figures 3b–3d. Radiances of ISS-LIS (red line) and GLM (black line) have been computed by integrating radiances from all the events detected every 2 ms frame (Figure 3c). Since both ISS-LIS and GLM observe the 777.4 nm spectral band, there is very high consistency with the same MMIA photometer spectral band (red line in Figure 3b). Note that ISS-LIS (red line) radiance stops before GLM (black line) because the flash was no longer in the field of view of the sensor.

Inspecting the photometer radiances (Figure 3b), after 442.05 s, the blue and red channels showed a progressive increase of radiance superimposed with small surges. At 442.15 s the red signal abruptly increased producing several peaks just before the +CG. This increase was also present in the GLM and ISS-LIS radiances. Just after the time of the +CG stroke, the peak was more pronounced in the red than in the blue band. The red pulse presented faster rise and decay times (2.2/12.9 ms) compared to the blue (5.4/71.1 ms). Starting right after the +CG stroke, the ELF magnetic field signal measured in Cape Verde (Figure 3–e) suggests the presence of continuing current. This continuing current is noticeable in the ELF signal for about 30 ms that corresponds to a decay to about 25% of the peak value in the MMIA red and GLM radiances.

The presence of continuing current during this period is also supported by the identified LMA sources of a fast ($0.4 \times 10^6 \text{ m s}^{-1}$) negative leader. Note that the transients in the magnetic field occurring after 442.25 s (Figure 3e) might belong to a different flash, according to the detection of a distant flash at that time by GLM. The small signal in the MMIA 180–230 nm photometer (Figure 3d), seems to present a small increase at the time of the +CG, and behaves more similarly to the blue band although its amplitude is more than three orders of magnitude smaller.

3.3. MMIA Imaging Data and Weather Radar

In the last four video frames recorded by MMIA, the flash was entirely in the field-of-view, so the previous frames have been omitted in this study. The periods of each video frame are indicated with vertical lines in Figure 3b and displayed in Figure 4. The four camera images of ASIM are shown in Figure 4 with the blue channel (337 nm) images in the left column and the red channel (777.4 nm) images in the right column. The location of the investigated boxes on the MMIA images can be easily identified in Figure 1c.

In the video frame 1 (Figure 4a), the luminosity of the flash comes from the location of the –CG stroke that occurred 125 ms before the frame start and where the LMA detected some negative leader breakdown activity (Box 1 in Figures 1b and 1c). During frame 1, the LMA detected a new leader propagating out of what will become the main luminosity core toward the east (Box 2). This new leader is seen in both cameras, but remained undetected by GLM and ISS-LIS. The radar cross sections along the LMA sources during this frame indicate that the sources occurred above the altitude of the 20 dBZ reflectivity echo tops. During frame 2, the leader entered into a more stratiform region (Box 2) with reflectivity <15 dBZ echo tops above the leader height (8 km) and coldest cloud top temperature of -67°C (13.5 km). The leader is clearly seen in both MMIA cameras (Figure 4b) and GLM reports events within the high radiance region in the red MMIA image. At the beginning of frame 3 (Figure 4c), a +CG stroke located in Box 1 triggered a fast negative leader ($0.4 \times 10^6 \text{ m s}^{-1}$) that propagated and branched during the frame exposure. The branch toward the south-east (Box 3) produced more LMA sources than the branch that propagated to the north (Box 4) but only the latter is well identified in the red image. Figure 4d depicts frame 4 where the leader propagating to the north-east (Box 5) can be more easily distinguished in the red image than in the blue. It is also remarkable that the section of leader end appears brighter than its channel behind. The north-east branch (Box 5) is responsible for the radiance peak after 442.25 s in the MMIA red channel photometer (Figure 3b) and GLM (Figure 3c), this will be discussed in section 4.2.

To relate cloud properties with the optical observations, two-dimensional histograms of radar reflectivity with height, contoured-frequency-by-altitude diagrams (CFAD) are computed along the leader propagation paths in Figure 1b and shown in Figure 5. Box 1 corresponds to the area where the CG strokes were located; and Box 2 includes the area within ± 1 radial gate (representing 750 m width) along the central leader channel mapped by the LMA during frames 1, 2 before it branches. Boxes 3 and 4 are analogous to Box 2 for south-east and north branches during frames 3 and 4, respectively; and the same in Box 5 of the leader branch toward the north-east. In each CFAD, the altitude of the leader is indicated by the heavy horizontal dashed line whereas the 50th and 90th percentiles of the cumulative reflectivity Z are indicated by the solid and dashed lines, respectively.

The LMA sources within Box 1 are located at an altitude of ~ 9 km (Figure 2). At this altitude, the CFAD (Figure 5a) shows a thinner region with weak Z values with 90% of the reflectivity below 18 dBZ. In this area, the maximum radiances of the flash in both spectral channels are found in frame 3 (Figure 4c) when the +CG stroke occurred. The peak in the measured red photometer is higher than the one recorded by the blue photometer. In the same region defined by Box 1, the blue signal surpasses the red after the continuing current during frame 5 (Figure 4d). In Box 2, the CFAD shows a shallow cloud above the leader height at ~ 8 km with 90% of the reflectivity below ~ 17 dBZ. This low reflectivity and the shallow cloud above the leader channel did not prevent the lightning leader at this location to be imaged in frames 1 and 2. Much higher reflectivity <23 dBZ is found above the south-west lightning leader channel in Box 3 that propagates at 7.5 km altitude. Although Box 3 has low cloud tops according to the radar and satellite images, and the lightning leader channel is close to the top, the high reflectivity above the channel is an indication of high concentration and/or large size of cloud particles. The dense cloud in Box 3 could be responsible for the almost undetectable luminosity from the lightning channels there. In Box 4, the north leader channel

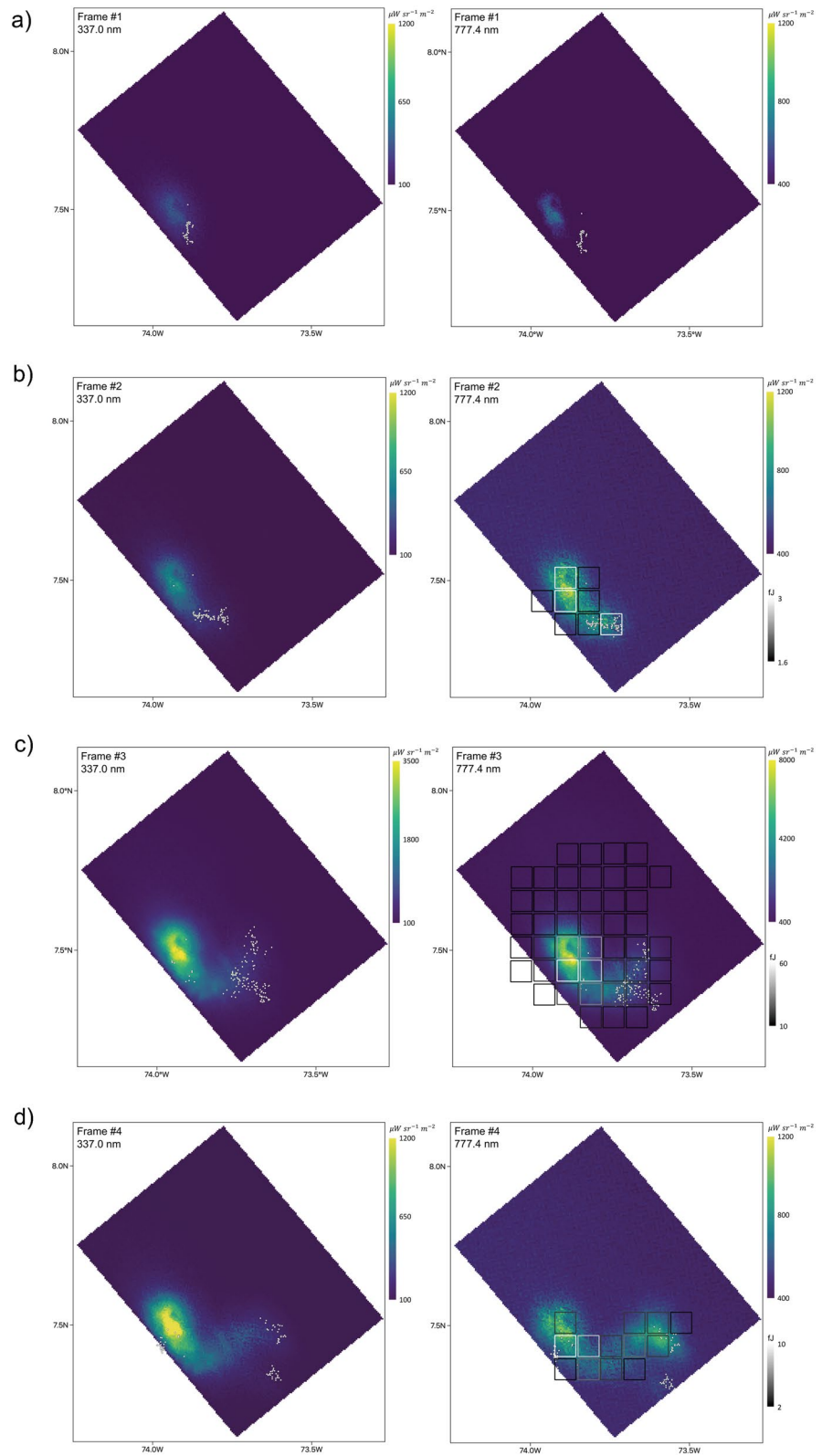


Figure 4. Consecutive MMIA camera frames in blue (337.0/4 nm) (left column) and red (777.4/5 nm) (right column) channels. LMA sources (white dots) are overlaid in each image. Locations of GLM events (gray squares) are plotted in the MMIA red images. GLM radiances (gray) at each location are integrated for the time of the frame. MMIA, The Modular Multispectral Imaging Array; LMA, Lightning Mapping Array; GLM, Geostationary Lightning Mapper.

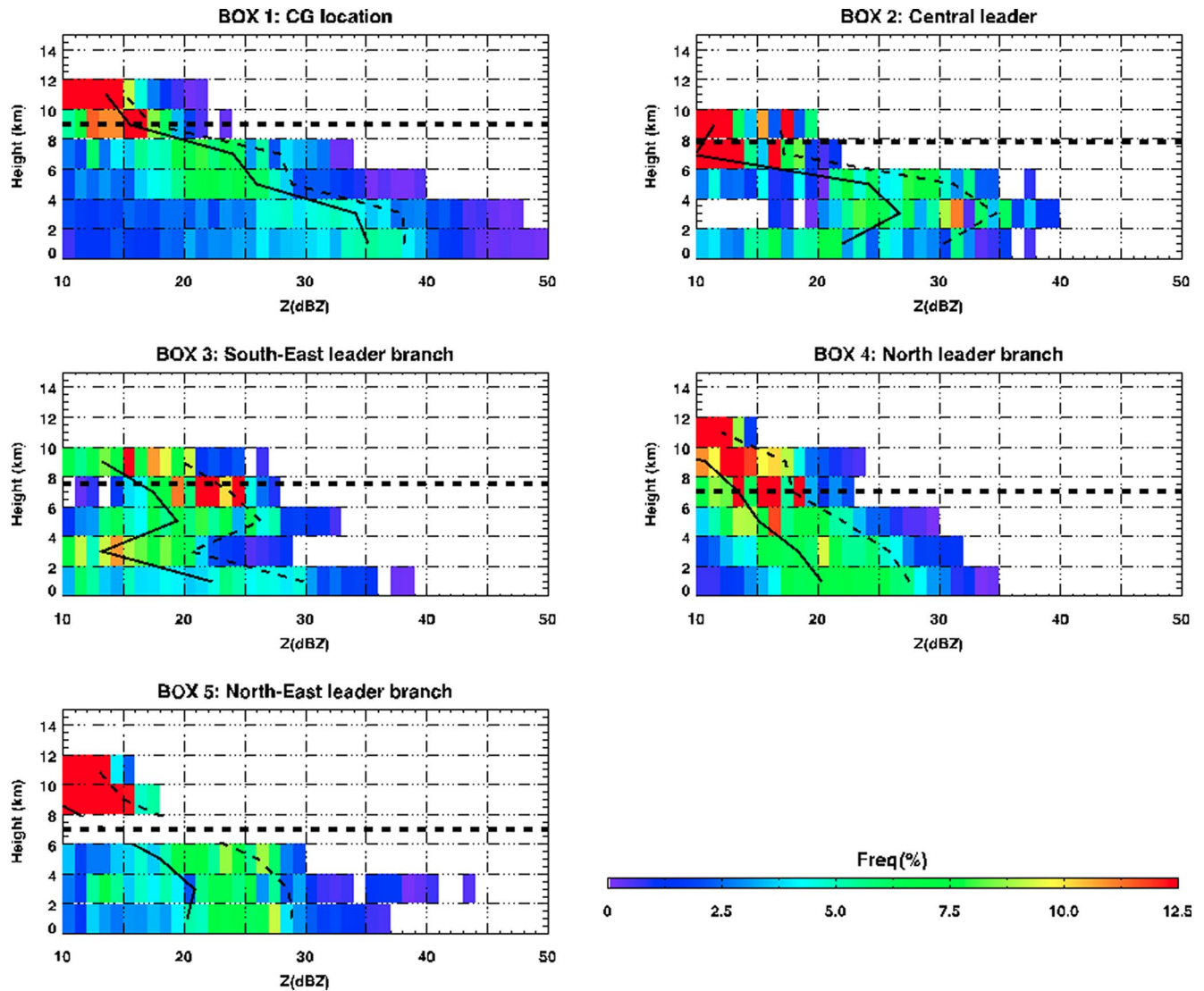


Figure 5. Reflectivity contoured-frequency-by-altitude diagram (CFAD). (a) Box 1: location of the CG strokes; (b) Box 2: central leader channel emerging from the location of the CG toward east; (c) Box 3: south-east leader branch; (d) Box 4 north leader branch; (e) Box 5: north-east leader branch. Horizontal heavy dashed line indicates the altitude of the leader sources in each box. Solid line marks the 50th percentile of the reflectivity Z and the dashed line the 90th percentile. CG, Cloud-to-ground.

propagates during frame 3 at an altitude of 7 km with a reflectivity of the cloud above it of <18 dBZ. In this area, luminosity of the leader is much higher in the red than in the blue image (Figure 3c). Finally, the cloud in Box 5 has convective characteristics as indicated by its cloud tops in Figure 1 and the reflectivity profile in Figure 5. The north-east leader in Box 5 during frame 4days is clear in the red image and well tracked by GLM, but highly attenuated and diffuse in the blue. The leader travels at 7 km and above this level we found reflectivity of <20 dBZ.

4. Discussion

4.1. Radiances and Radar Reflectivity

The average blue (337.0 nm) and red (777.4 nm) radiances observed by the ASIM cameras of the five selected boxes are shown in Figure 6.

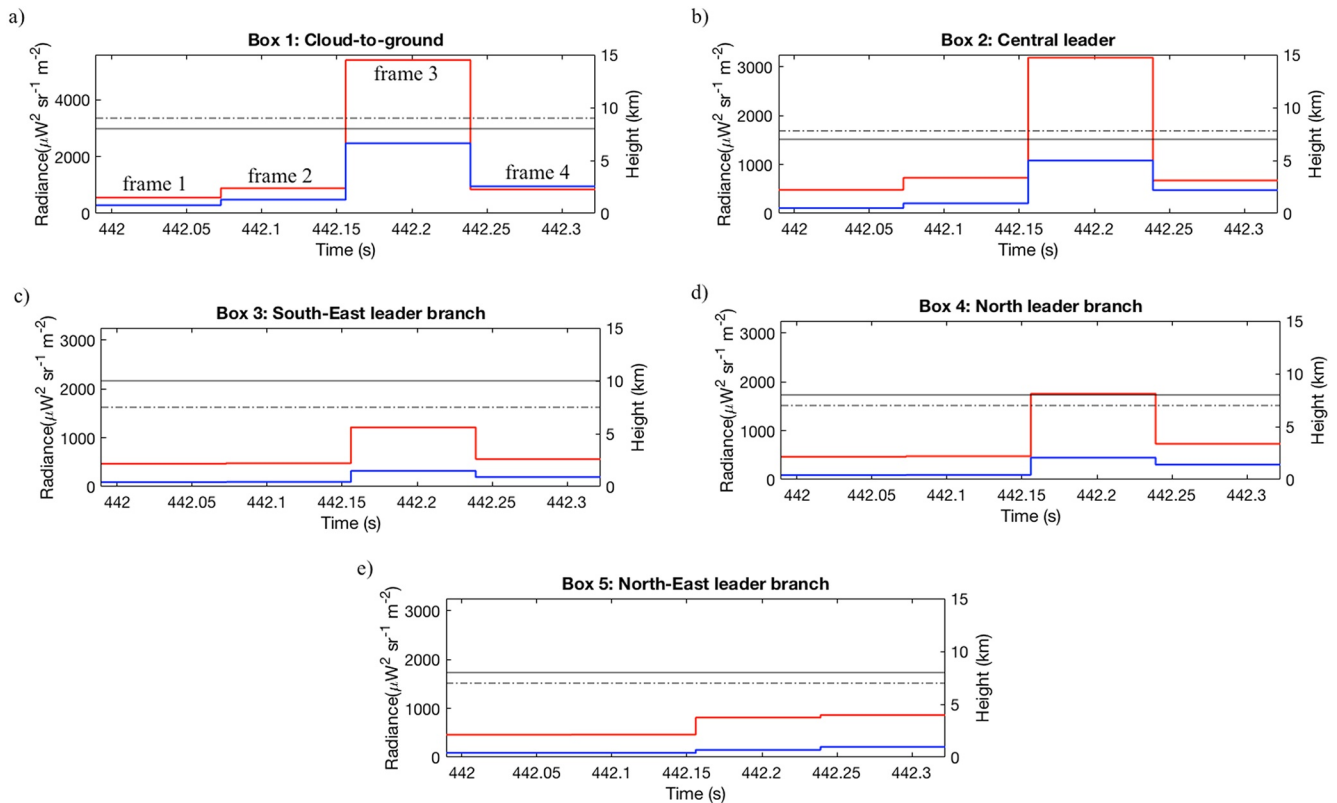


Figure 6. Average radiance of the blue (337.0 nm) and red (777.4 nm) from video frames for the Boxes 1–5. Dot-dash line indicates the altitude of the leader in each box. Solid line corresponds to the 20 dBZ radar echo top.

At the location of the CG strokes (Box 1), lightning leader sources are identified at an altitude of ~ 9 km with a shallow cloud of low reflectivity (< 18 dBZ) above it. This may have produced little attenuation compared to other deeper areas. The ratio of the received red to blue starts with values from ~ 1.85 during the frames 1 and 2 before the +CG stroke. At the time of the +CG stroke (frame 3), radiances peak and the ratio increases to 2.2. The ratio remains higher than one for the 30 ms corresponding to the continuing current phase until both radiances equalize. Later, in frame 4, the ratio of the average radiance decreases to 0.9 (0.6 for the peak radiances not shown in Figure 6), meaning that the received blue radiance is more intense than the red. From Figures 3 and 4, the consistency of the red radiance with the continuing current suggests that the observed red channel (777.4 nm) oxygen atomic line is more related with the evolution of lightning currents than the blue band. The relation of red radiance pulses with impulsive lightning current events identified by the LMA was previously observed by Thomas et al. (2000). In the laboratory, Windmar et al. (1991) found a proportional relation of the peak amplitude of the red radiance with the kiloampere current of a long spark. The relation of the 777.4 nm emission is related with hot lightning channels ($> 4,000$ K) or sparks that provide thermal excitation of the 5P electronic state of atomic oxygen (see the interpretation in Soler et al., 2020). In Box 1, the slow decay of the blue signal different to the red may indicate the prevalence of streamer/corona or other low temperature discharge activity, in particular, at the region of the location of the CG strokes. So, whereas the reduction of the red emission has been related to the decay of the continuing current, the prevalent blue optical emissions are assumed to come from the streamer/corona accompanying the high-altitude negative leader channel at this region. This channel is the root of the channels progressing along the other boxes. Blue emissions are common in streamer and corona discharges and are related to the N_2 second positive system and the N_2^+ first negative system (e.g., Soler et al., 2020 and references therein). In the laboratory, works such as Machala et al. (2011) and Janda et al. (2016) showed the emission of the N_2 second positive system at the 337.0 nm being associated with the streamer phase of a spark discharge. So, the identified prevalence of the blue signal might be related to the evolution of the electric fields related with the leaders and the cloud.

The radiance in Box 2 includes the leader channel emerging from the location of the CG strokes at frame 1. This negative leader propagated at 10^5 m s^{-1} and ended at the time of the +CG (frame 3). From this central leader channel two branches occurred after the +CG corresponding to the LMA sources in Boxes 3 and 4. At the time of frame 3, the central leader channel presented higher red radiance than its south-east, north and north-east branches in Boxes 3–5, respectively. As seen in Figures 5 and 6, at the regions of the south-east (Box 3), north (Box 4), and north-east (Box 5), the cloud above the leader was thicker in terms of reflectivity than in Box 2. This thicker cloud mostly affected the blue band. This is reflected in the ratios of the average radiance in Figures 5b–5e at the time of frame 3 corresponding to 2.9 (18 dBZ), 3.8 (23 dBZ), 4 (18 dBZ), and 5.4 (20 dBZ), respectively. The reflectivity in parentheses correspond to the maximum above the leader. During this frame, the charge that feeds the continuing currents to ground is assumed to be provided by the south and north leader branches based on the fast propagation ($0.4 \times 10^6 \text{ m s}^{-1}$) of the leaders and their higher radiances compared to the extension of the north-east leader.

One of the salient features of the observation is the imaged north-east leader branch (Box 5) by the red camera at frame 4 (Figure 4d). This leader end produced an increase in the 777.4 nm radiance after 442.25 s (Figure 3b) which is not observed in the blue channel image. The level of the blue radiance in Box 5 during frame 4 corresponds almost to the background level and it is lower than the corresponding radiance at the same frame but in the leader channel behind in Box 2. For comparison, the red radiance during frame 4 is ~ 1.2 times greater in Box 5, at the leader end, compared to its trailing channel in Boxes 4 and 2 although Box 5 had the deepest cloud above the leader. This negative correlation between the radiance and radar reflectivity suggests that the detected surge in the radiation might be related with the occurrence of some intracloud process involving high currents (e.g., recoil leader event) at the leader end in Box 5.

In addition, taking into account that the used weather radar is more sensitive to the back-scatter of ice and water particles and these precipitating ice particles are related to icy cloud particles (Baker et al., 1999), it is plausible to state that the higher the ice content above 8 km the higher will be the concentration of cloud ice particles. Moreover, the broader the CFAD distributions above the freezing level, the more ice cloud particles are produced reflecting higher updrafts that consequently produce more supersaturation. Therefore, the optical emissions would be more attenuated depending on the concentration and the size of ice particles above the leader (Brunner & Bitzer, 2020; Rutledge et al., 2020) as well as on the water vapor (Thomason & Krider, 1982) that fed those particles. At Box 3, the higher and large sized ice cloud particles concentration attenuated both the red and blue channels, while at Boxes 4 and 5, the presence of more water vapor and smaller ice cloud particles might have contributed to enough attenuation of both spectral bands. The north and north-east leaders (Boxes 4 and 5) may have produced sufficiently high currents to generate detectable levels of red emissions. In Section 4.3, a quantitative analysis of the cloud optical depths at the considered regions is presented.

In summary, the red radiance is close related to the occurrence of the currents on the leader channels according to the identified CG strokes, continuing currents and the recoil leader event consistently with previous works (e.g., Thomas et al., 2000). The longer time decay of the blue emissions relative to the red and their lower correlation with the evolution of the currents can be indicative that these blue emissions are related to the streamer zones of the leader channels according to the nature of the blue emission (N_2 second positive system). So, blue emissions would be related to the evolution of the electric fields of the leader and the cloud. Nevertheless, the detected blue radiation allows imaging of the leader channels in the regions with less cloud above the lightning flash.

4.2. Surges of Radiance Associated With Leader Branching

The small surges in red and blue emissions at 442.127 s in Figure 3b during frame 2 (marker e) are related to a new branch of the developing leader. This branch continues for 40 ms until the time of the +CG stroke. This leader branch can be associated with the downward positive leader approaching the ground, including the last 12 ms where both the blue and red radiances increased, oscillating in the red. This oscillation is consistent with the impulsive optical emissions by recoil leader events (K-changes) analyzed by (Montanyà et al., 2012) using high speed video during the development of positive leader to ground. Impulsive red optical emissions related to recoil leader events were previously reported by Thomas et al. (2000). About 50 ms after the +CG stroke (frame 3), at 442.226 s, a new radiance surge in the red channel is associated

Table 1
Relative Optical Depth of the Cloud Section Above the Lightning Leader Channels up to 10 km

	Relative optical depth
Box 1	1
Box 2	0.5
Box 3	2
Box 4	0.9
Box 5	0.9

Note. Optical depths are relative to Box 1.

with new negative leader branches (from g and h in Figure 2) propagating for 20 ms with speeds $0.4 \times 10^6 \text{ m s}^{-1}$ (Boxes 3 and 4). Finally, the red surge at 442.256 s in frame 4, Box 5, also occurred in association with a leader branching and further propagation (i-j in Figure 2). In the blue photometer, these surges are unnoticed at the indicated times although there are some smoothed and delayed pulses that might be related. This is the case of the peak in the blue at 442.226 s occurring 7 ms after the peak in the red (Figure 3b). If both peaks are related, then the significant delay might be due to the blue radiance originating from the region of the CG stroke (Box 1) whereas the red originates from the location of the leader branching (Boxes 3 and 4). Possible delays due to higher scattering in the blue than in the red are possible (e.g., Luque et al., 2020).

4.3. Optical Depth

Light et al. (2001) and Beirle et al. (2014), among others, stated that clouds mostly affect the propagation of light causing spatial smearing via multiple scattering. Light absorption by ice and water at the 337.0 and 777.4 nm is small (e.g., Light et al. 2001; Thomason & Krider, 1982; Warren, 1984; Warren & Brandt, 2008) but the absorption and scattering differences can be significant between the two wavelengths (Luque et al., 2020). Some previous works (e.g., Brunner & Bitzer, 2020; Koshak et al., 1994; Light et al. 2001; Thomas et al., 2000; Thomason & Krider, 1982) found that the optical depth between the light source and the cloud edges including the horizontal extension of the cloud (Koshak et al., 1994) highly affects the detectability of lightning. These works also indicate the need to know the location and the progression of the source within the cloud. Rutledge et al. (2020) found that optical emissions are not completely correlated with the ice water path above individual lightning flashes derived from radar data because the precipitating particles detected by radar are not necessarily the main reason for the light attenuation. Small undetectable cloud particles may have higher concentrations and so can produce collectively higher light attenuation than precipitation-size particles.

We now attempt to evaluate the effects of the cloud on the light propagation at the investigated regions of the flash. Due to the radar limitations, we adopt the cloud particle distribution from vertical radar reflectivity and temperature profiles using the parametrization by Heymsfield et al. (2002, 2013). The calculated particle distributions at each level are limited from a minimum diameter of 20 μm up to a parametrized maximum diameter. Optical depth of the cloud sections above the lightning leader channels at each box are calculated by following Thomason and Krider (1982). Optical depths are limited up to an altitude of 10 km because, as pointed out by Rutledge et al. (2020), we found unrealistically high particle densities for the low temperatures at higher levels. Details on the calculations of particle distribution and optical depth are provided in the Appendix A of this article. Results of the estimated optical depths are presented in Table 1. The values are relative to the optical depth in Box 1. We present relative optical depths because of the high sensitivity of the cloud particle distribution on the temperature (Heymsfield et al., 2002, 2013). Despite this dependence, the relative optical depths between boxes remain almost independent to temperature offsets. The calculated relative optical depths are consistent with some of the characteristics of the observed radiance from each box. The lower optical depth of Box 2 relative to Box 1 is in accordance with the more stratiform nature of the cloud in this region where the red and blue radiances were less effected by cloud. The reduction of 50% of the optical depth in Box 2 results from the decrease of 3 dBZ and a shallower cloud above the leader compared to Box 1. In contrast, Box 3 presents the highest relative optical depth ~ 2 coinciding with the region with the almost undetected blue and red radiances. Compared to Box 1, despite the fact that the median reflectivity above the leader is 1 dBZ higher, the maximum reflectivity (90th percentile) is 6 dBZ greater and with lower lightning leader channel height. In between, the 0.9 relative optical depth of Box 5 allowed the detection of the red emissions but strongly attenuated the blue. Figure 1a shows a higher cloud top in Box 5 if compared to Box 4 and similar to the cloud tops in Box 1. The median reflectivity in Box 5 at the leader altitude is 2 dBZ lower than in Box 1 whereas the reflectivity corresponding to the 90th percentile is 3 dBZ higher.

In summary, to overcome the limitation of radar on the detection of cloud particles the parametrized ice particle size distributions employed have provided consistent relative optical depth with the optical observations. Consistently with Brunner and Bitzer (2020), the results highlight the importance on the combination of the light emission by different lightning processes and the optical depth features due to cloud ice particles surrounding the lightning channels at high cloud altitudes (>7 km). The location at Box 1 where the return stroke currents produced high channel luminosity and with low cloud optical depth due to lightning channels at high altitudes, would be evidence of the CG features pointed out by Zhang and Cummins (2020) to produce high detection efficiency of CG flashes by GLM. In the area of the lowest relative optical depth (Box 2) corresponding to a stratiform region, the propagation of negative lightning leaders has been optically resolved by MMIA and GLM. The detection of this leader by GLM might have been made possible by the occurrence of a branching of the leader that produced a surge in the radiance (marker e in Figure 3b) if compared to the undetected leader by GLM in frame 1 (Figure 4a). The increase of a factor of two on the relative optical depth in Box 3 attenuated the optical emissions of a fast negative leader producing abundant LMA sources. The undetected leader did not present any feature such as branching or recoil leader that might have involved a surge in channel luminosity. Box 5 with lower optical depth than Box 1 and a surge in radiance, allowed GLM to image the propagation of the leader (Figure 4-d) all along the channel from the tip to the location of the former CG. Our results complement the recent study by Rutledge et al. (2020). Instead of using the ice water path derived from radar and cloud top path (liquid plus ice) we have estimated the cloud particle size distribution from parametrization data and we have found consistency with the observations. In addition, we have investigated the features in different parts of the flash considering their cloud and lightning features. Nevertheless, for a precise evaluation of the light escaping from the cloud, cloud edges and the horizontal cloud extension (Koshak et al., 1994) should not be omitted.

5. Conclusions

We have presented concurrent measurements of a lightning flash from space by ASIM, GLM, ISS-LIS and from the ground by the Colombia-LMA, WWLLN, a local weather radar, and an ELF electromagnetic wave receiver. This observation has provided the means for interpretation of the optical observations with respect to lightning leader processes. This flash included negative and positive strokes as well the occurrence of continuing currents. In addition, weather radar data allowed estimation of the attenuation of optical radiance by the clouds above the lightning leaders at different locations along the path of the lightning channel propagation.

5.1. The following Summarizes Our Findings:

- Surges in the photometer radiance, especially in red (777.4 nm), besides return stroke and recoil leader processes have been found to be associated with lightning leader branching involving new leader development. These surges associated to leader branching are not always noticed in the blue (337.0 nm) signals, so these processes appear not to involve significant emissions in this wavelength
- The radiance at red correlates with the continuing current identified from the magnetic ELF signals, the fast leader development detected by the LMA and the continuous radiance
- The oscillations in the red signal photometer just before the +CG stroke are probably recoil leader events during the downward propagation of the leader to ground prior to the return stroke
- Based on the above, the detected red signals are likely from the highly conducting hot leader channels and associated with high luminosity of the channel involving impulsive and continuing current processes
- The camera images showed long persistence of blue radiation at the location of the +CG stroke after the decay of the continuing current and even surpassing the detected red radiance
- The blue emission has been shown to not be closely related to lightning current processes. The nature of the N_2 second positive system optical emission suggests the origin from nonthermal discharges (streamers) on the leader channels and probably in the thundercloud
- The detected blue radiation allowed imaging of the leader channels especially in the stratiform areas with low cloud tops

- Cloud depth or cloud thickness above the lightning channels appears to attenuate more to the blue emission more than the red
- Relative optical depths at different parts of the cloud where lightning leaders propagated have been estimated from radar and temperature data using parametrized models of particle size distribution
- Besides the position of the lightning leaders and the properties of the cloud above and around them, detection of optical emissions of lightning depends on the different lightning processes, which can be inferred from their temporal and spectral properties

Appendix A

Heymsfield et al. (2002, 2013) have presented assimilation of experimental data to provide ice particle size distributions. One of the common functional forms of the particle size distribution $N(D)$ is the gamma function:

$$N(D) = N_{o\Gamma} D^\mu e^{-\lambda_\Gamma D} \quad (\text{cm}^{-4})$$

where D is the particle diameter, $N_{o\Gamma}$ is the intercept, λ_Γ is the slope, and μ is the shape. The last three parameters are derived from radar and temperature variables as presented by Heymsfield et al. (2002). The simplified equation for the intercept:

$$N_{o\Gamma} = \frac{Z \lambda_\Gamma^{(5.5+\mu)}}{1.210^8 \Gamma(5.5 + \mu)}$$

where Z is the radar reflectivity factor ($\text{mm}^6 \text{m}^{-3}$) converted from observed weather radar measuring in dBZ. Taking into account the use of a C-Band weather radar and measurements above the 0 °C, Z can be expressed as (Heymsfield et al., 2002):

$$Z = 10^{\left(\frac{\text{dBZ}+7.2}{10}\right)}$$

where 7.2 dBZ is to correct the ice/water dielectric constant effect. To simplify, we adopt the median dBZ reflectivity at each level shown in Figure 5. The slope λ_Γ and the shape μ are estimated from the median fitted functions in Heymsfield et al. (2002), respectively:

$$\lambda_\Gamma = 24 e^{-0.049T} \quad (\text{cm}^{-1})$$

$$\mu = 0.13 \lambda_\Gamma^{0.64} - 2$$

where T is the temperature in °C. The maximum diameter for each distribution is calculated according to the region of the cloud. For Boxes 1 and 5, the maximum diameter is selected for convective type (Heymsfield et al., 2013):

$$D_{\max} = 2.1 e^{0.070T} \quad (\text{cm})$$

whereas for the stratiform areas in Box 2, Box 3, and Box 5:

$$D_{\max} = 1.1 e^{0.069T} \quad (\text{cm})$$

In the lower part of the distribution D has been limited to 20 μm . Once the fitted gamma functions $N(D)$ are obtained, photon mean free paths are calculated according to Thomason and Krider (1982):

$$\Lambda \approx \frac{1}{\int_{D_{\min}}^{D_{\max}} \pi D^2 N(D) dD}$$

Finally, the optical depth τ is calculated according to the corresponding geometric deepness L of the given reflectivity region above the lightning channel

$$\tau = \frac{L}{\Lambda}$$

With the available data and the presented calculations, we cannot provide a precise estimation of the optical depth. From our experience some of the aspects to consider in the future are:

- (1) Better radar vertical resolution is convenient. Here we cannot resolve levels higher than 10 km for all the regions of the flash, because the radar has been configured to monitor rain mainly
- (2) By increasing the number of elevations or scanning continuous vertical cross sections (like sector range height indicator—RHI) with a polarimetric radar, like this one, polarimetric variables like differential radar reflectivity (ZDR), specific differential phase (K_{DP}) and correlation coefficient among horizontal and vertical polarization can be augmented to estimate the type of ice particles and its size (Liu & Chandrasekar, 2000)
- (3) C-band radars detect mostly precipitation-size particles. The referenced works allow to extend to lower size particles, even to the few μm size. However, we have found that at temperatures lower than -40°C (~ 11 km) the density of low sized particles increases several orders of magnitude providing very dense clouds that result in an increase of the optical depth by an order of magnitude. A similar unrealistic effect is found by Rutledge et al. (2020) in relation of the temperature dependence of the intercept parameter

Despite the assumptions and limitations, the relative optical depths presented in Table 1 present a reasonable agreement with the observed luminosity features in each box.

Data Availability Statement

Data associated with this work are available at <https://zenodo.org/record/4530914>. Data access to ASIM is available by registering at <https://asdc.space.dtu.dk/>. GLM data are available from NOAA (GOES-R Series Program, 2019, <https://data.nodc.noaa.gov/cgi-bin/iso?id=gov.noaa.ncdc:C01527#>) and ISS-LIS from NASA Global Hydrology Resource Center (Blakeslee et al., 2019, <https://ghrc.nsstc.nasa.gov/pub/lis/iss/data/science/nqc/hdf/>). The ABI imagery can be accessed from the NOAA's Comprehensive Large Array Storage Service (CLASS) or the Google (gcp-public-data-goes-16) or Amazon cloud.

Acknowledgments

This work was supported by research grants from the Spanish Ministry of Economy and the European Regional Development Fund (FEDER): ESP2013-48032-C5-3-R, ESP2015-69909-C5-5-R, ESP2017-86263-C4-2-R, and PID2019-109269RB-C42. ASIM is a mission of ESA's SciSpace Program for scientific utilization of the ISS and non-ISS space exploration platforms and space environment analogs. It is funded by ESA and national contributions through contracts with TERMA and Technical University of Denmark (DTU) in Denmark, University of Bergen (UB) in Norway, and University of Valencia (UV) in Spain. The ASIM Science Data Center (ASDC) at DTU is supported by PRODEX contract PEA 40001 1 5884. The authors are grateful to Keraunos for providing LINET lightning data and the World-Wide Lightning Location Network (<http://wwlln.net/>) for providing WWLLN lightning location data. Also, we would like to thank the Colombian Instituto de Hidrología, Meteorología y Estudios Ambientales (IDEAM) for providing the weather radar information used in this study.

References

- Aranguren, D., López, J., Inampués, J., Torres, H., & Betz, H. D. (2017). Cloud-to-ground lightning activity in Colombia and the influence of topography *Journal of Atmospheric and Solar-Terrestrial Physics*, 154, 182–189. <https://doi.org/10.1016/j.jastp.2016.08.010>
- Baker, M. B., Blyth, A. M., Christian, H. J., Latham, J., Miller, K. L., & Gadian, A. M. (1999). Relationships between lightning activity and various thundercloud parameters: Satellite and modeling studies. *Atmospheric Research*, 51, 221–236.
- Beirle, S., Koshak, W., Blakeslee, R., & Wagner, T. (2014). Global patterns of lightning properties derived by OTD and LIS. *Natural Hazards and Earth System Sciences*, 14, 2715–2726.
- Betz, H. D., Schmidt, K., & Oettinger, W. (2009). *LINET—An International VLF/LF lightning detection network in Europe. Lightning: principles, instruments and applications*. Dordrecht: Springer. https://doi.org/10.1007/978-1-4020-9079-0_5
- Bitzer, P. M. (2017). Global distribution and properties of continuing current in lightning. *Journal of Geophysical Research: Atmospheres*, 122, 1033–1041. <https://doi.org/10.1002/2016JD025532>
- Blakeslee, R. J. (2019). *Non-Quality Controlled Lightning Imaging Sensor (LIS) on International Space Station (ISS) Science Data*. Huntsville, AL: NASA EOSDIS Global Hydrology Resource Center Distributed Active Archive Center. <https://doi.org/10.5067/LIS/ISSLIS/DATA107>
- Blakeslee, R. J., Lang, T. J., Koshak, W. J., Buechler, D., Gatlin, P., Mach, D. M., et al. (2020). Three years of the lightning imaging sensor onboard the International Space Station: Expanded global coverage and enhanced applications. *Journal of Geophysical Research: Atmospheres*, 125, e2020JD032918. <https://doi.org/10.1029/2020JD032918>
- Boccippio, D. J., Koshak, W. J., & Blakeslee, R. J. (2002). Performance assessment of the optical transient detector and lightning imaging sensor. Part I: Predicted diurnal variability. *Journal of Atmospheric and Oceanic Technology*, 19, 1318–1332.
- Boccippio, D. J., Williams, E. R., Heckman, S. J., Lyons, W. A., Baker, I. T., & Boldi, R. (1995). Sprites, ELF transients, and positive ground strokes. *Science*, 269, 1088.
- Brunner, K. N., & Bitzer, P. M. (2020). A first look at cloud inhomogeneity and its effect on lightning optical emission. *Geophysical Research Letters*, 47, e2020GL087094. <https://doi.org/10.1029/2020GL087094>
- Burke, C. P., & Jones, D. L. (1996). On the polarity and continuing currents in unusually large lightning flashes deduced from ELF events. *Journal of Atmospheric and Terrestrial Physics*, 58, 531.

- Cáceres-Leon, R. (2017). *Meteorología Aplicada a la Seguridad de las Operaciones Aéreas*. Colección Ciencia y Poder Aéreo. Retrieved from <https://libros.publicacionesfac.com/index.php/libros/catalog/book/22>
- Chanrion, O., Neubert, T., Lundgaard Rasmussen, I., Stoltze, C., Tcherniak, D., Jessen, N. C., et al. (2019). The modular multispectral imaging array (MMIA) of the ASIM Payload on the International Space Station. *Space Science Reviews*, 215, 28. <https://doi.org/10.1007/s11214-019-0593-y>
- Christian, H. J., Blakeslee, R. J., & Goodman, S. J. (1989). The detection of lightning from geostationary orbit. *Journal of Geophysical Research*, 94, 13329–13337.
- Dee, D. P., Uppala, S. M., Simmons, A. J., Berrisford, P., Poli, P., Kobayashi, S., & Bechtold, P. (2011). The ERA—Interim reanalysis: Configuration and performance of the data assimilation system. *Quarterly Journal of the Royal Meteorological Society*, 137(656), 553–597.
- Erdmann, F., Defer, E., Caumont, O., Blakeslee, R. J., Pédeboy, S., & Coquillat, S. (2020). Concurrent satellite and ground-based lightning observations from the optical lightning imaging sensor (ISS-LIS), the LF network Meteorage and the SAETTA LMA in the northwestern Mediterranean region. *Atmospheric Measurement Techniques*, 13, 853–875.
- GOES-R Algorithm Working Group and GOES-R Series Program. (2018). NOAA GOES-R Series Geostationary Lightning Mapper (GLM) Level 2 lightning detection: Events, groups, and flashes. NOAA National Centers for Environmental Information. <https://doi.org/10.7289/V5KH0KK6>
- Goodman, S. J., Blakeslee, R. J., Koshak, W. J., Mach, D., Bailey, J., Buechler, D., et al. (2013). The GOES—R geostationary lightning mapper (GLM). *Atmospheric Research*, 125–126, 34–49.
- Heymsfield, A. J., Bansemer, A., Field, P. R., Durden, S. L., Stith, J., Dye, J. E., et al. (2002). Observations and parameterizations of particle size distributions in deep tropical cirrus and stratiform precipitating clouds: Results from in situ observations in TRMM field campaigns. *Journal of the Atmospheric Sciences*, 59, 3457–3491.
- Heymsfield, A. J., Schmitt, C., & Bansemer, A. (2013). Ice cloud particle size distributions and pressure-dependent terminal velocities from in situ observations at temperatures from 0° to –86°C. *Journal of the Atmospheric Sciences*, 70, 4123–4154.
- Huang, E., Williams, E., Boldi, R., Heckman, S., Lyons, W., Taylor, M., et al. (1999). Criteria for sprites and elves based on Schumann resonance observations. *Journal of Geophysical Research*, 104, 16943–16964.
- Koshak, W. J., Solakiewicz, R. J., Phanord, D. D., & Blakeslee, R. J. (1994). Diffusion model for lightning radiative transfer. *Journal of Geophysical Research*, 99, 14361–14371.
- Light, T. E., Szczymski, D. M., Kirkland, M. W., & Jacobson, A. R. (2001). Simulations of lightning optical waveforms as seen through clouds by satellites. *Journal of Geophysical Research*, 106, 17103–17114.
- Liu, H., & Chandrasekar, V. (2000). Classification of Hydrometeors Based on Polarimetric Radar Measurements: Development of Fuzzy Logic and Neuro-Fuzzy Systems, and In Situ Verification. *The Journal of Atmospheric and Oceanic Technology*, 17, 140–164. [https://doi.org/10.1175/1520-0426\(2000\)017<0140:COHBOP>2.0.CO;2](https://doi.org/10.1175/1520-0426(2000)017<0140:COHBOP>2.0.CO;2)
- López, J. A., Montanyà, J., van der Velde, O. A., Pineda, N., Salvador, A., Romero, D., et al. (2019). Charge structure of two tropical thunderstorms in Colombia. *Journal of Geophysical Research: Atmospheres*, 124, 5503–5515. <https://doi.org/10.1029/2018JD029188>
- Luque, A., Gordillo-Vázquez, F. J., Li, D., Malagón-Romero, A., Pérez-Invernón, F. J., Schmalzried, A., et al. (2020). Modeling lightning observations from space-based platforms (CloudScat.jl 1.0). *Geoscientific Model Development*. <https://doi.org/10.5194/gmd-2020-161>
- Montanyà, J., van der Velde, O. A., March, V., Romero, D., Solà, G., & Pineda, N. (2012). High-speed video of lightning and X-ray pulses during the 2009–2010 observation campaigns in northeastern Spain. *Atmospheric Research*, 117, 1–132. <https://doi.org/10.1016/j.atmosres.2011.09.013>
- Montanyà, J., van der Velde, O. A., Pineda, N., & López, J. A. (2019). ISS-LIS data analysis based on LMA networks in Europe. Darmstadt: EUMETSAT Science Studies. Retrieved from <https://www.eumetsat.int/website/home/Data/ScienceActivities/ScienceStudies/ISSLIS-DataAnalysisBasedonLMANetworksinEurope/index.html#OB>
- Neubert, T., Østgaard, N., Reglero, V., Blanc, E., Chanrion, O., Oxborrow, C. A., et al. (2019). The ASIM mission on the International Space Station. *Space Science Reviews*, 215, 26. <https://doi.org/10.1007/s11214-019-0592-z>
- Peterson, M. (2019). Using lightning flashes to image thunderclouds. *Journal of Geophysical Research: Atmospheres*, 124, 10175–10185. <https://doi.org/10.1029/2019JD031055>
- Peterson, M. J. (2014). *Variations of optical and radio lightning characteristics and the relationship between storm convective intensity and above—Cloud electric fields*. (Dissertation). Salt Lake City, UT: The University of Utah. Retrieved from <https://search.proquest.com/openview/2d481bb6a222ae8958de1016fd602870/1?pq-origsite=gscholar&cbl=18750&diss=y>
- Rison, W., Thomas, R., Krehbiel, P., Hamlin, T., & Harlin, J. (1999). A GPS-based three dimensional lightning mapping system: Initial observations in central New Mexico. *Geophysical Research Letters*, 26, 3573–3576.
- Rodger, C. J., Werner, S., Brundell, J. B., Lay, E. H., Thomson, N. R., et al. (2006). Detection efficiency of the VLF World-Wide Lightning Location Network (WWLLN): Initial case study. *Annales Geophysicae, European Geosciences Union*, 24(12), 3197–3214.
- Rudlosky, S., Goodman, S. J., and Virts, K. S. (2019a). *Lightning detection: Geostationary Lightning Mapper, The GOES-R series: A new generation of geostationary environmental satellites*. Netherlands: Academic Press. <http://www.worldcat.org/oclc/1127541502>
- Rudlosky, S. D., Goodman, S. J., Virts, K. S., & Bruning, E. C. (2019b). Initial geostationary lightning mapper observations. *Geophysical Research Letters*, 46, 1097–1104. <https://doi.org/10.1029/2018GL081052>
- Rutledge, S. A., Hilburn, K. A., Clayton, A., Fuchs, B., & Miller, S. D. (2020). Evaluating geostationary lightning mapper flash. *Journal of Geophysical Research: Atmospheres*, 125. e2020JD032827. <https://doi.org/10.1029/2020JD032827>
- Soler, S., Perez-Invernón, F. J., Gordillo-Vázquez, F. J., Luque, A., Li, D., Malagón-Romero, A., et al. (2020). Blue optical observations of narrow bipolar events by ASIM suggest corona streamer activity in thunderstorms. *Journal of Geophysical Research: Atmospheres*, 125, e2020JD032708. <https://doi.org/10.1029/2020JD032708>
- Stuhlmann, R., Rodriguez, A., Tjemkes, S., Grandell, J., Arriaga, A., Bézy, J.-L., et al. (2005). Plans for EUMETSAT's third generation Meteosat Geostationary Satellite Program. *Advances in Space Research*, 36(5), 975–981.
- Thomas, R. J., Krehbiel, P. R., Rison, W., Hamlin, T., Boccippio, D. J., Goodman, S. J., & Christian, H. J. (2000). Comparison of ground based 3-dimensional lightning mapping observations with satellite-based LIS observations in Oklahoma. *Geophysical Research Letters*, 27, 1703–1706. <https://doi.org/10.1029/1999GL010845>
- Thomas, R. J., Krehbiel, P. R., Rison, W., Hunyady, S., Winn, W., Hamlin, T., & Harlin, J. (2004). Accuracy of the lightning mapping array. *Journal of Geophysical Research*, 109, D14207. <https://doi.org/10.1029/2004JD004549>
- Thomason, L. W., & E. P. Krider (1982). The effects of clouds on the light produced by lightning. *Journal of the Atmospheric Sciences*, 39, 2051–2065.
- van der Velde, O., Montanyà, J., Neubert, T., Chanrion, O., Lopez, J. A., Fabro, F., et al. (2020). Comparison of high-speed optical observations of a lightning flash from space and the ground. *Earth and Space Science*, 7, e2020EA001249. <https://doi.org/10.1029/2020EA001249>

- van der Velde, O. A., & Montanyà, J. (2013). Asymmetries in bidirectional leader development of lightning flashes. *Journal of Geophysical Research: Atmospheres*, *118*, 13504–13519. <https://doi.org/10.1002/2013JD020257>
- van der Velde, O. A., Montanyà, J., Soula, S., Pineda, N., & Mlynarczyk, J. (2014). Bidirectional leader development in sprite-producing positive cloud-to-ground flashes: Origins and characteristics of positive and negative leaders. *Journal of Geophysical Research D: Atmospheres*, *119*, 12755–12779. <https://doi.org/10.1002/2013JD021291>
- Warren, S. G. (1984). Optical constants of ice from the ultraviolet to the microwave. *Applied Optics*, *23*, 1206–1225.
- Warren, S. G., & Brandt, R. E. (2008). Optical constants of ice from the ultraviolet to the microwave: A revised compilation. *Journal of Geophysical Research*, *113*, D14220. <https://doi.org/10.1029/2007JD009744>
- Yang, J., Zhang, Z., Wei, C., Lu, F., & Guo, Q. (2017). Introducing the new generation of Chinese Geostationary Weather Satellites, Fengyun—4. *Bulletin of the American Meteorological Society*, *98*(8), 1637–1658. <https://doi.org/10.1175/BAMS-D-16-0065.1>
- Yuter, S. E., & Houze, Jr., R. A. (1995). Three-dimensional kinematic and microphysical evolution of Florida cumulonimbus. Part II: Frequency distributions of vertical velocity, reflectivity, and differential reflectivity. *Monthly Weather Review*, *123*, 1941–1963.
- Zhang, D., and Cummins, K. L. (2020). Time evolution of satellite-based optical properties in lightning flashes, and its impact on GLM flash detection. *Journal of Geophysical Research: Atmospheres*, *125*. e2019JD032024. <https://doi.org/10.1029/2019JD032024>